Dissipative solitary waves in a two-dimensional complex plasma: Amorphous versus crystalline

He Huang,[1] Alexei V. Ivlev,[2] Volodymyr Nosenko,[3] Wei Yang,[1] and Cheng-Ran Du[1,4,*]

[1]*College of Science, Donghua University, Shanghai 201620, People's Republic of China*

[2]*Max Plank Institute for Extraterrestrial Physics, Garching 85748, Germany*

[3]*Institut für Materialphysik im Weltraum, Deutsches Zentrum für Luft- und Raumfahrt (DLR), Cologne 51147, Germany*

[4]*Member of Magnetic Confinement Fusion Research Centre, Ministry of Education, Shanghai 201620, People's Republic of China*

(Received 6 January 2023; accepted 22 March 2023; published 26 April 2023)

The propagation of a dissipative soliton was experimentally studied in a two-dimensional binary complex plasma. The crystallization was suppressed in the center of the particle suspension where two types of particles were mixed. The motions of individual particles were recorded using video microscopy, and the macroscopic properties of the solitons were measured in the amorphous binary mixture in the center and in the plasma crystal in the periphery. Although the overall shape and parameters of solitons propagating in amorphous and crystalline regions were quite similar, their velocity structures at small scales as well as the velocity distributions were profoundly distinct. Moreover, the local structure rearranged drastically in and behind the soliton, which was not observed in the plasma crystal. Langevin dynamics simulations were performed, and the results agreed with the experimental observations.

DOI: 10.1103/PhysRevE.107.045205

I. INTRODUCTION

Amorphous particle suspensions at low temperature exhibit remarkable features [1]. For example, the long-time α relaxation represents the structural rearrangement and is separated from the short-time β relaxation, which is caused by the caging motion [2,3]. The minor changes in the local structure may lead to a huge increase in viscosity as temperature decreases [4,5]. The mechanical rigidity is accompanied by the dynamic heterogeneity [6,7]. Such systems have been widely studied in colloids, granular matters, and complex plasmas [8–10].

A complex plasma is composed of a weakly ionized gas and negatively charged microparticles [11,12]. In the laboratory, monodisperse particles form a single layer in the (pre)sheath above the powered electrode of a gas discharge and can self-organize in a triangular lattice with hexagonal symmetry, known as a plasma crystal [13,14]. Recently, the formation of other lattice structures, such as a square lattice was predicted and realized experimentally [15,16]. The crystallization can be suppressed upon fast cooling in the binary complex plasmas, when two types of microparticles are mixed in a (quasi)-two-dimensional (2D) suspension [17,18]. A major part of such a particle suspension exhibits a disordered structure, and the dispersion relation of the particle oscillations has distinct features [19,20]. The configurational temperature can be directly measured, and the computation of the entropy change upon heating and cooling of the system yields good agreement with Dulong-Petit law [21,22].

Complex plasmas can be externally excited in the experiments. Shear flows, Mach cones, melting, and other phenomena can be triggered electrically by the powered wires or optically by the laser beams [23–29]. As one of the most significant phenomena, the propagation of the solitary waves in the complex plasmas has been extensively studied in the past years [30]. A soliton is a wave isolated in space which retains the shape when it propagates through the medium. In the three-dimensional complex plasmas, the dissipative dark solitons were observed, and the propagation of solitons at an interface in the phase-separated complex plasmas was studied [31–34]. In the 2D plasma crystals, solitons were excited by powered wires and the collisions of solitons were studied experimentally and numerically [35,36]. However, to date, there has been no investigations on the solitons in the quasi-2D amorphous complex plasmas.

In this paper, we report on the experimental investigations on the propagation of the dissipative solitary wave in a 2D binary complex plasma. Despite the fact that the macroscopic properties of the soliton are similar in the amorphous binary mixture and in the crystal, the microscopic structure of the wave profile and the relaxation of the particles demonstrate drastically distinct features. The experimental observations are compared with the Langevin dynamics (LD) simulations.

II. EXPERIMENT

The experiments were performed in a modified gaseous electronics conference (GEC) rf reference cell [18,37,38]. Argon plasma was generated with a capacitively coupled rf discharge at 13.56 MHz at a gas pressure of 0.65 Pa. The negatively charged particles were levitated in the sheath above the bottom electrode where the gravity force was balanced by the electric force. The particles were illuminated by a horizontal laser sheet from the side, and their movements were recorded by a complementary metal-oxide semiconduc-

*chengran.du@dhu.edu.cn

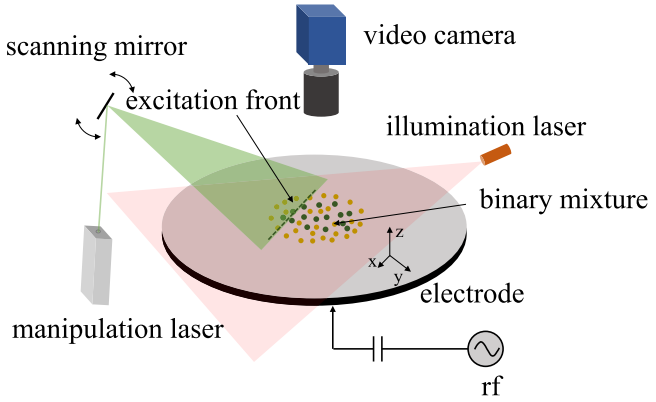

FIG. 1. Sketch of the experimental setup with a modified GEC chamber. Microparticles were illuminated by a horizontal laser sheet (red) and imaged by a fast video camera from the top. A manipulation laser beam was spread by a scanning mirror and formed another laser sheet (green). The laser was powered for 1 s, and a solitary wave was excited close to the periphery of the particle suspension, propagating in the y direction.

tor video camera from the top at 125 frames per second as depicted in Fig. 1. The melamine formaldehyde (MF) particles with a diameter of 9.19 μm and the polystyrene (PS) particles with a diameter of 11.36 μm were injected into the plasma consecutively; below we refer to them as "small" and "big" particles, respectively. Their masses were $m_{\mathrm{MF}} = 6.1 \times 10^{-13}$ and $m_{\mathrm{PS}} = 8.0 \times 10^{-13}$ kg.

Particle positions were determined using the moment method to achieve the subpixel resolution [39,40]. In principle, the small and big particles can be distinguished based on the size and intensity of recorded bright spots (representing individual particles) in the image due to different particle sizes and materials [41]. However, the light intensity of the illumination laser sheet was slightly inhomogeneous, it was difficult to accurately identify the particle types in a substantial area with a nonuniform background in the image.

Based on the horizontal phonon spectra of the corresponding crystalline suspensions under equivalent discharge conditions [42], the particle charges were estimated as $Q_{\mathrm{MF}} \approx 10\,800e$, $Q_{\mathrm{PS}} \approx 16\,500e$, and the effective plasma screening length was $\lambda_D \approx 0.5$ mm. We note that the vertical vibration frequency of the particles in the sheath was measured as ~30 Hz based on the intensity oscillation of the scattered light recorded by the video camera from the top [43]. Thus, the length scale of the electric field gradient E/E' at the equilibrium position could be estimated as ~0.28 mm [44]. As a result, the charge ratio between the small and the big particles may be increased by up to 50% in comparison with the size ratio due to the present vertical distance between the two layers. As shown in Fig. 2, the mean horizontal interparticle distance of $\Delta \approx 0.5$ mm was directly measured from the first peak of the pair correlation function $g(r)$, leading to a screening parameter of $\kappa = \Delta/\lambda_D \approx 1$.

A binary mixture was formed in the central area of the circular suspension with a disordered structure. The MF particles were levitated slightly higher than the PS particles. Their vertical separation was about one quarter of the horizontal interparticle distance, measured by a side view camera.

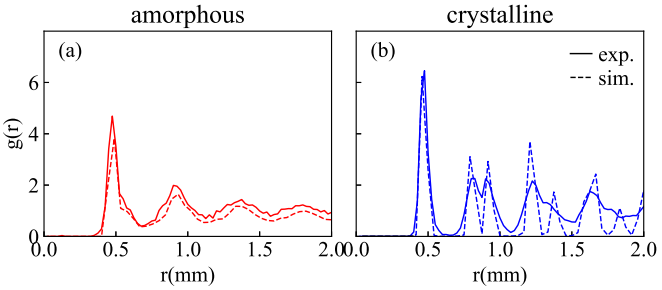

FIG. 2. Pair correlation function $g(r)$ in the (a) amorphous binary mixture and the (b) plasma crystal.

In the sheath, the trajectories of the ions were bent by the negatively charged particles and the ion wakes were formed downstream in the ion flow [45–47]. As a result, the interaction between the MF and PS particles was no longer reciprocal in the binary mixture [48,49]. In the periphery, the MF particles self-organized and formed a plasma crystal. The particle suspension slowly rotated, which might be induced by the inhomogeneity of the illumination laser intensity profile [18]. The angular speed was $\omega \sim 10^{-3}$ rad/s, which was much smaller than the speed of the solitary wave.

The solitary wave was excited by a manipulation laser [50,51]. The laser beam with a wavelength of 532 nm was expanded into a sheet by a scanning mirror that oscillated rapidly at 200 Hz and was pointed toward the suspension at a grazing angle, see Fig. 1. The laser power was set at a moderate value $P_L = 10$ W. The resulting radiation pressure of the laser light pushed the particles and launched the soliton, propagating in the positive y direction [52] as shown in Fig. 3. Here, the laser was powered on for 1 s for the excitation, so that the solitary wave had a certain magnitude but did not melt the binary mixture. In the present paper, we compare the propagation of the soliton in the amorphous binary mixture (central area) and the crystal (periphery) in the same particle suspension.

III. SIMULATION

The LD simulations with the same two types of particles were performed to study the propagation of the solitary wave in the amorphous binary mixture. The equation of motion including damping reads

$$m_i \ddot{\boldsymbol{r}}_i + m_i \nu_i \dot{\boldsymbol{r}}_i = \sum_j \boldsymbol{F}_{ji} + \boldsymbol{F}_{c,i} + \boldsymbol{L}_i, \tag{1}$$

where $\boldsymbol{r}_i$ is the position of particle i, m_i is the mass, ν_i is the damping rate, $\boldsymbol{F}_{ji}$ is the interparticle interaction force, $\boldsymbol{F}_{c,i}$ is the confinement force in the z directions, and $\boldsymbol{L}_i$ represents the Langevin heat bath. The Langevin force $\boldsymbol{L}_i(t)$ is defined by $\langle \boldsymbol{L}_i(t) \rangle = 0$ and $\langle \boldsymbol{L}_i(t) \boldsymbol{L}_i(t+\tau) \rangle = 2\nu_i m_i T\, \delta(\tau)\mathbf{I}$, where T is the temperature of the heat bath, $\delta(\tau)$ is the δ function, and $\mathbf{I}$ is the unit matrix. The damping rates were set $\nu_{\mathrm{PS}} = 0.91$ and $\nu_{\mathrm{MF}} = 0.77\ \mathrm{s}^{-1}$ for the PS and MF particles, respectively, same as in the experiments.

The microparticles were randomly scattered in a simulation box with a size of 24×96 mm^2. We set periodic boundary conditions in the x direction and the harmonic potential wall

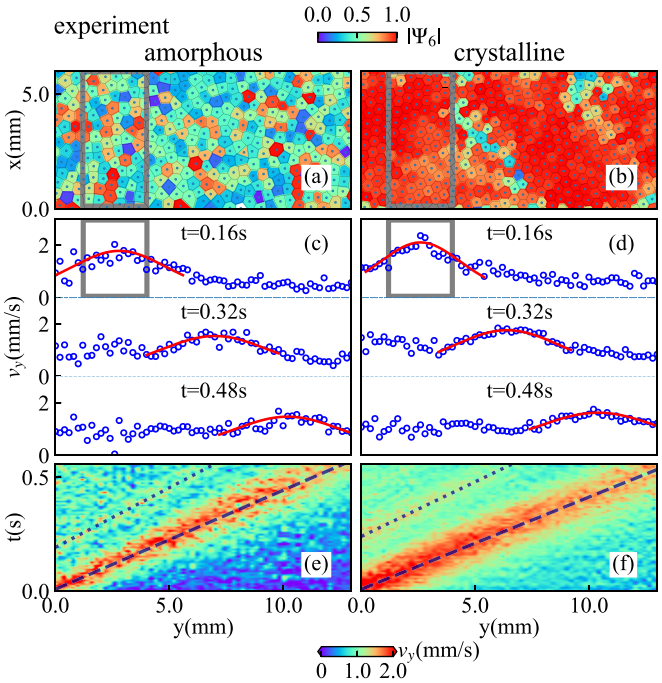

FIG. 3. Propagation of solitons in the experiments with the amorphous binary mixture (left) and the plasma crystal (right). The structure was characterized by the hexatic order parameter Ψ_6 in panels (a) and (b). The location of the soliton at $t = 0.16$ s is highlighted by the gray rectangles. The particle velocities v_y in the soliton at three selected times were fitted by the soliton solution in panels (c) and (d). The propagation of the solitons is shown in panels (e) and (f). The soliton speed C was obtained by the fit to the solitons according to Eq. (3) (dashed line) and the constant sound speed C_s was obtained by the linear fit to the secondary pulse (dotted line).

boundary conditions in the y direction. In the binary mixture, the two types of particles were separately confined by the parabolic confinement in the z direction where the equilibrium height differed by $H = 140$ μm. Here, the strength of this parabolic confinement was set so that the vertical motion could be drastically suppressed. The small and big particles virtually moved in the layers at their respective equilibrium height. The interparticle interaction of the Yukawa point-wake model was used in the simulation [19,53]. The force F_{ji} exerted on particle i by particle j was composed of the repulsive force $\boldsymbol{F}^p_{ji}$ by particle j and the attractive force $\boldsymbol{F}^w_{ji}$ by the pointlike wake charge q_j below particle j with a distance of $\delta = 40$ μm as depicted in Fig. 4. The net effective force thus can be written as

$$\boldsymbol{F}_{ji} = \boldsymbol{F}^p_{ji} + \boldsymbol{F}^w_{ji} = Q_i Q_j f(r_{ji}) \frac{\boldsymbol{r}_{ji}}{r_{ji}} + Q_i q_j f\left(r^w_{ji}\right) \frac{\boldsymbol{r}^w_{ji}}{r^w_{ji}}, \quad (2)$$

where $f(r) = \exp(-r/\lambda_D)(1 + r/\lambda_D)/r^2$, $\boldsymbol{r}_{ji} = \boldsymbol{r}_i - \boldsymbol{r}_j$, and $\boldsymbol{r}^w_{ji} = \boldsymbol{r}_i - (\boldsymbol{r}_j - \delta \boldsymbol{e}_z)$. The simulations were performed using LAMMPS in the NVT ensemble [54,55]. The kinetic temperature was set to 2000 K. The charge ratio was set $q_i/Q_i = 0.2$.

After the system was relaxed, an excitation force $F_L = -65y^2 + 250$ pN was applied to the particles within the range of $-2 < y < 2$ mm located close to the left end of the simulation box for 10 ms. The solitary wave was excited and

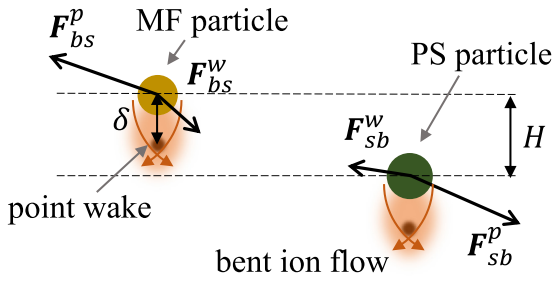

FIG. 4. Sketch of the point-wake model in a binary particle suspension in the plasma sheath. The ion flow is bent due to the presence of the negatively charged particle, resulting in a nonreciprocal interaction between the MF (small) and PS (big) particles. Here, F^p_{bs} is the repulsive force exerted on the small particle from the big particle itself and F^w_{bs} is the attractive force from the (point) wake of the big particle (and similar for the force exerted on the big particle). Note that $|F^p_{bs}| = |F^p_{sb}|$ whereas $|F^w_{bs}| \neq |F^w_{sb}|$.

evolved in y direction, similar as in the experiments. The results are shown in Fig. 5. For comparison, similar simulation was also performed separately for a plasma crystal composed of monodisperse MF particles.

IV. RESULTS

The difference between the structures of the particle suspensions can be demonstrated by the pair correlation function, as shown in Fig. 2. In the plasma crystal, the first peak exceeds

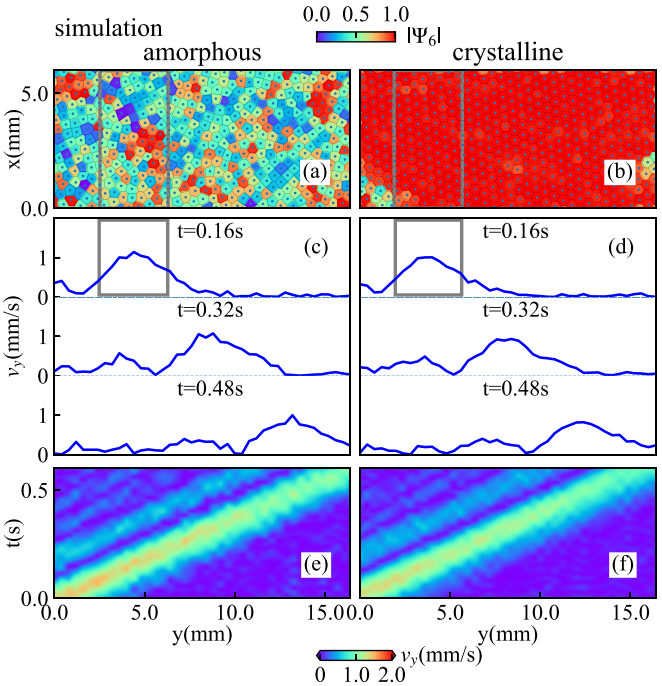

FIG. 5. Propagation of solitons in the simulations with the amorphous binary mixture (left) and the plasma crystal (right). Similar as in Fig. 3, the hexatic order parameter Ψ_6 at $t = 0.16$ s is shown in panels (a) and (b), whereas the particle velocities v_y at $t = 0.16$, 0.32, and 0.48 s are plotted in panels (c) and (d). The propagation of the solitons is shown in panels (e) and (f).

a value of 6, whereas a double-peak feature is clearly visible at $r \sim 0.8$ mm, reflecting an ordered hexagonal structure. On the contrary, in the amorphous binary mixture, the value of the first peak is drastically reduced, and the double peak structure for the secondary neighbors vanished. The ordered structure was suppressed by the mixture of two types of particles. Moreover, as the distance between big particles was slightly larger than that between small particles, the width of the first peak was broadened as shown in Fig. 2(a).

The local structure of the particle suspension can also be quantified by the hexatic order parameter $\Psi_6(\boldsymbol{r}) = \frac{1}{6}\sum_{m=1}^{6} e^{i6\theta_m}$, where six nearest neighbors were considered, and θ_m was the angle between $(\boldsymbol{r}_m - \boldsymbol{r})$ and the x axis. As shown in Fig. 3(a), the binary mixture effectively suppressed the formation of hexagonal lattice structure, whereas in the monodisperse plasma crystal $|\Psi_6(\boldsymbol{r})|$ approaches unity with a few defects, see Fig. 3(b). As the amplitude of the excitation was moderate, the crystalline structure was not destroyed at the position of the soliton where the particles were accelerated and obtained high values of v_y. Similar distribution of the $|\Psi_6(\boldsymbol{r})|$ can also be observed in the simulations as shown in Fig. 5. Note that in the plasma crystal, there were significantly fewer defects in the simulations than in the experiments.

The dimensionless amplitude A and the width L of the solitary wave can be obtained by fitting the particle velocity profile v_y to the soliton solution $v_y = CA\,\cosh^{-2}(\xi/L)$, where $\xi = y - Ct$ is a self-similar variable and C is the soliton speed. As shown in Figs. 3(c) and 3(d), the amplitude A decreased drastically with time as the soliton propagated, whereas the width L rose gradually. The relations between the soliton parameters A, L, and the Mach number $M = C/C_s$ can be expressed as [35]

$$M^2 - 1 = 4l_d^2/L^2 = -\Lambda A/3, \tag{3}$$

where l_d is the dispersion length and Λ is the dimensionless nonlinearity coefficient, see Ref. [35] for details.

The propagation of the solitary wave in the amorphous binary mixture can be seen in the space-time plot in Fig. 3(e) where the color represents the velocity v_y averaged over the x direction. The constant sound speed $C_s \approx 20$ mm/s was directly measured by the linear fit to the pulse (dotted line) behind the soliton [35,56], whereas the soliton speed $C \approx 24$ mm/s and the Mach number $M \approx 1.2$ were obtained by the fit to the soliton (dashed line) according to Eq. (3). In fact, the solitary wave was so weak that the compression could be marginally seen in Fig. 3(a) at $t = 0.16$ s where the wave front was enclosed in the gray rectangle. Similar propagation was also seen in the plasma crystal as shown in Fig. 3(f).

The evolution of the amplitude and the width of the soliton is shown in Fig. 6. The experimental and simulation results are plotted as symbols and lines, respectively. In the weakly damped case, both the amplitude and the width scale exponentially,

$$A \propto \exp(-2\nu t/3), \quad L \propto \exp(\nu t/3), \tag{4}$$

as derived in Ref. [35] for $M - 1 \ll 1$. As a result, the fitted damping rate shows that the dissipation was mainly caused by the neutral gas friction and the damping rate was comparable ($\nu \sim 1$ s^{-1}) in the amorphous binary mixture and the plasma crystal [35]. Therefore, despite that the interparticle distance

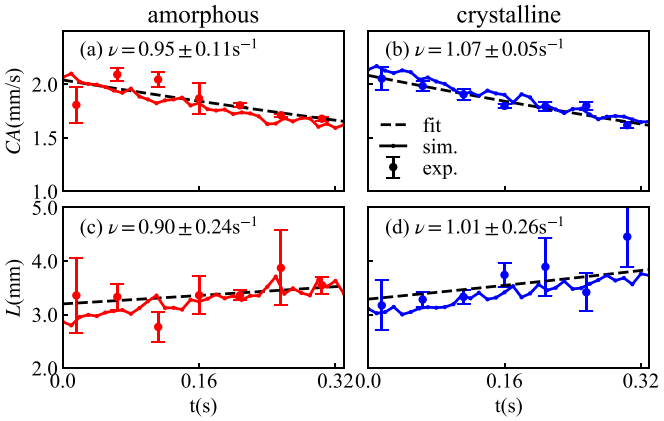

FIG. 6. Evolution of the soliton amplitude A (a) and (b) and the soliton width L (c) and (d) in the amorphous binary mixture and plasma crystal, respectively. The experimental results are shown by symbols and the simulation results by curves. They were fitted by exponential functions according to Eq. (4) as shown by the dashed lines, resulting in the damping rates.

in the binary mixture was marginally larger due to the presence of the big particles, the propagation characteristics of the soliton can be directly compared in the two cases.

However, the spatial profile of the soliton in the amorphous binary mixture is rather different from that in the plasma crystal. The particle motions in the two cases are illustrated and compared in Figs. 7(a) and 7(b). To highlight the spatial profile of the soliton, the outline of the particles, whose velocities v_y exceed the averaged value, was determined using the α shape algorithm [57–59]. As expected, the soliton front

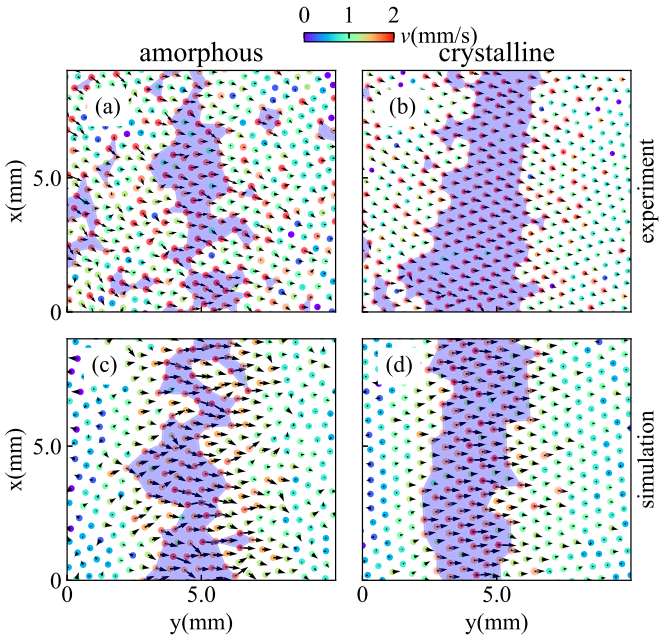

FIG. 7. Velocity structure of the solitons in the amorphous binary mixture (a) and (c) and in the plasma crystal (b) and (d). The arrows and the color represent the velocity of individual particles at $t = 0.32$ s. The light blue areas show the α shape constructed based on the particles, whose velocities exceed the averaged value.

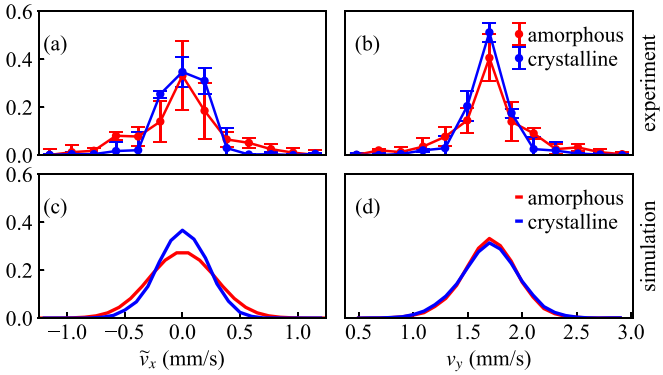

FIG. 8. Distribution of the particle velocity perpendicular (a) and (c) and parallel (b) and (d) to the propagation direction of the soliton. The distributions in the experiments were obtained by measuring the particle velocities in 10 frames around $t = 0.32$ s where the error represents the standard deviation. $\tilde{v}_x$ was shifted by $\langle v_x \rangle$ so that their mean value equals zero for easy comparison.

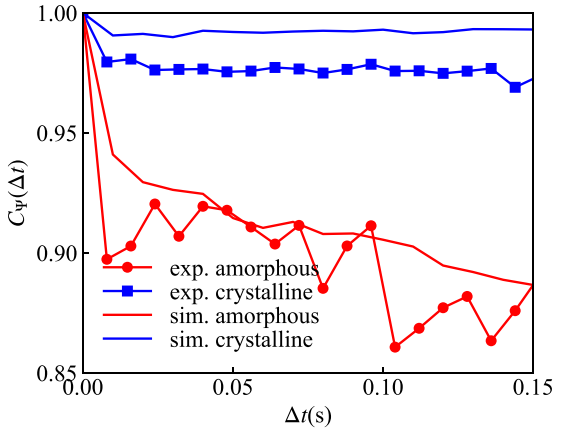

FIG. 9. Evolution of the BOC function $C_\Psi(\Delta t)$ in the experiments and simulations. As the BOC function drops marginally for the plasma crystal, the disordered structure in the binary mixture leads to a rearrangement as the soliton disturbs the particles, indicated by the significant drop of the BOC function.

had a rather flat shape in the plasma crystal, signifying the synchronized motions of the particles in the ordered structure. On the contrary, due to the distinct local structures of the amorphous binary mixture, the particles moved in different directions with various velocities in the soliton, resulting in an irregular outline. The front exhibited convex and concave shapes, and several patches might be identified. Similar phenomena were also observed in the numerical simulations as shown in Figs. 7(c) and 7(d).

The features can also be demonstrated by the velocity distribution in the soliton. We plot the distribution of the particle velocity parallel and perpendicular to the propagation direction within the width of the soliton in Fig. 8. As we see in Fig. 8(a), the distribution of $\tilde{v}_x$ had a fatter tail in the amorphous binary mixture, which resulted from the irregular motions of the particles. This feature was also clearly visible in the simulation as shown in Fig. 8(c). Note that $\tilde{v}_x$ was shifted by $\langle v_x \rangle$ so that their mean value equals zero for easy comparison. Here, the nonzero $\langle v_x \rangle$ in the experiment was caused by the slow rotation of the whole suspension, which vanished in the numerical simulation. In contrast, v_y had a similar distribution in the two cases.

The propagation of the soliton had a strong impact on the rearrangement of the local structure. Here, we extended the local order parameter as $\Psi_{n_j} = \frac{1}{n_j} \sum_{m=1}^{n_j} e^{i n_j \theta_m}$, where n_j is the number of the neighboring particles around particle j. Instead of six neighbors, here the number of neighbors was a variable, determined by the Delaunay triangulation algorithm. The parameter quantifies how evenly the neighboring particles are distributed, signifying the rigidness of the local structure. Furthermore, a bond-orientational correlation (BOC) function was defined to quantify the structural rearrangement [60–62] as

$$C_\Psi(\Delta t) = \left\langle \sum_j^N \Psi_{n_j}^*(t) \Psi_{n_j}(t + \Delta t) \right\rangle_t \Big/ \left\langle \sum_j^N |\Psi_{n_j}(t)|^2 \right\rangle_t \quad (5)$$

for N particles in a certain area within the soliton width, where Δt was the waiting time counting from the moment that the soliton left this area of interest. As shown in Fig. 9, $C_\Psi(\Delta t)$ decayed marginally at the very beginning and stayed at a plateau afterwards in the plasma crystal. The propagation of the weak soliton barely changed the local structure. However, in the amorphous binary mixture, the situation was rather different. The BOC function decreased rapidly from unity to ∼0.9 within the first 0.02 s. It further dropped with a slower pace and reached a plateau at $\Delta t \sim 0.15$ s. The local structure was dramatically disturbed by the soliton and the

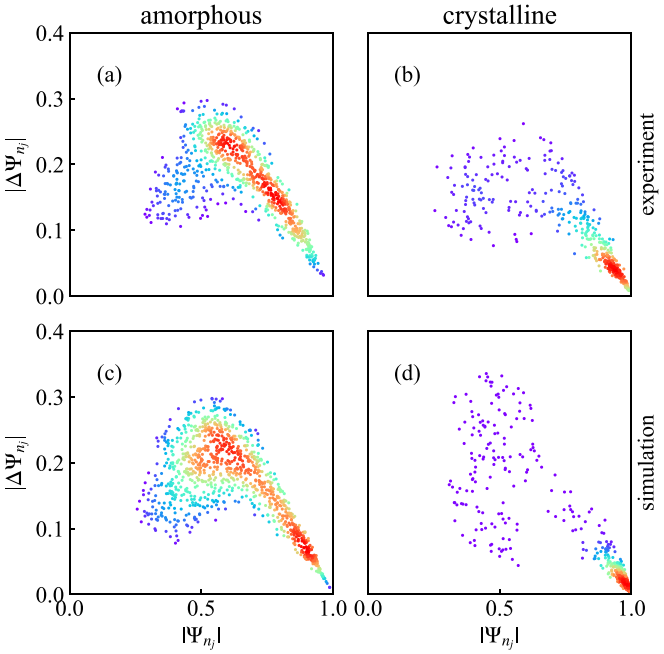

FIG. 10. Change in the local order parameter $|\Delta\Psi_{n_j}|$ at the waiting time $\Delta t = 0.15$ s. The color represents the density of the symbols where red indicates high density. In the amorphous binary mixture, the change in the local structure mainly occurred where the local structures were relatively unstable, signified by a substantial reduction in $|\Psi_{n_j}|$.

particles rearranged themselves both in the experiments and simulations.

In order to find the particles susceptible to the disturbance, we plot the change in the local order parameter $|\Delta\Psi_{n_j}|$ for the particles with a constant waiting time of $\Delta t = 0.15$ s. The results are shown in Fig. 10. On the one hand, as the majority of the particles had the ordered structure with $|\Psi_{n_j}| > 0.9$ in the plasma crystal, their changes $|\Delta\Psi_{n_j}|$ were smaller than 0.1. On the other hand, $|\Psi_{n_j}|$ was widely spread from 0.4 to 1 in the amorphous binary mixture. The change $|\Delta\Psi_{n_j}|$ was significantly larger. Note that for a small portion of the particles with neighbors evenly distributed around them ($|\Psi_{n_j}| \sim 1$) [18], the change $|\Delta\Psi_{n_j}|$ was insignificant. This shows that for the particles with the rigid local structure, the rearrangement can be vastly suppressed, even in the amorphous binary mixture.

V. CONCLUSIONS

In this paper, we report on the experimental and numerical investigations of the propagation of the dissipative soliton wave in a 2D amorphous binary complex plasma and plasma crystal. The soliton was excited by a laser pulse; the dissipation was due to the neutral gas friction. The macroscopic properties of the soliton propagation were similar in the two cases. However, the microscopic structure of the soliton exhibited a tortuous outline in the binary mixture due to the disordered local structure. Furthermore, as demonstrated by the BOC function, the particles dramatically rearranged themselves as the soliton propagated in the amorphous complex plasma, which was not observed in the plasma crystal. Our results shed light on the wave phenomena in the strongly coupled amorphous particle suspension.

ACKNOWLEDGMENTS

This work was supported by the National Natural Science Foundation of China (NSFC), Grants No. 11975073 and No. 12035003 and the Fundamental Research Funds for the Central Universities, Grant No. 2232023G-10. We thank N. Xu and H. M. Thomas for valuable discussions.

[1] L. Berthier and M. D. Ediger, Phys. Today **69**(1), 40 (2016).
[2] D. R. Reichman and P. Charbonneau, J. Stat. Mech.: Theory Exp. (2005) P05013.
[3] E. R. Weeks, J. C. Crocker, A. C. Levitt, A. Schofield, and D. A. Weitz, Science **287**, 627 (2000).
[4] P. G. Debenedetti and F. H. Stillinger, Nature (London) **410**, 259 (2001).
[5] G. L. Hunter and E. R. Weeks, Rep. Prog. Phys. **75**, 066501 (2012).
[6] W. K. Kegel, and A. van Blaaderen, Science **287**, 290 (2000).
[7] A. S. Keys, A. R. Abate, S. C. Glotzer, and D. J. Durian, Nat. Phys. **3**, 260 (2007).
[8] L. Berthier and G. Biroli, Rev. Mod. Phys. **83**, 587 (2011).
[9] S. R. Nagel, Rev. Mod. Phys. **89**, 025002 (2017).
[10] A. Ivlev, H. Löwen, G. Morfill, and C. P. Royall, *Complex Plasmas and Colloidal Dispersions: Particle-Resolved Studies of Classical Liquids and Solids* (World Scientific, Singapore, 2012).
[11] V. Fortov, A. Ivlev, S. Khrapak, A. Khrapak, and G. Morfill, Phys. Rep. **421**, 1 (2005).
[12] G. E. Morfill and A. V. Ivlev, Rev. Mod. Phys. **81**, 1353 (2009).
[13] J. H. Chu and L. I, Phys. Rev. Lett. **72**, 4009 (1994).
[14] H. Thomas, G. E. Morfill, V. Demmel, J. Goree, B. Feuerbacher, and D. Möhlmann, Phys. Rev. Lett. **73**, 652 (1994).
[15] A. V. Zampetaki, H. Huang, C.-R. Du, H. Löwen, and A. V. Ivlev, Phys. Rev. E **102**, 043204 (2020).
[16] S. Singh, P. Bandyopadhyay, K. Kumar, and A. Sen, Phys. Rev. Lett. **129**, 115003 (2022).
[17] F. Wieben, J. Schablinski, and D. Block, Phys. Plasmas **24**, 033707 (2017).
[18] C.-R. Du, V. Nosenko, H. M. Thomas, Y.-F. Lin, G. E. Morfill, and A. V. Ivlev, Phys. Rev. Lett. **123**, 185002 (2019).
[19] H. Huang, A. V. Ivlev, V. Nosenko, Y.-F. Lin, and C.-R. Du, Phys. Plasmas **26**, 013702 (2019).
[20] P. Hartmann, Z. Donkó, G. J. Kalman, S. Kyrkos, K. I. Golden, and M. Rosenberg, Phys. Rev. Lett. **103**, 245002 (2009).
[21] F. Wieben, D. Block, M. Himpel, and A. Melzer, Phys. Rev. E **104**, 045205 (2021).
[22] F. Wieben and D. Block, Phys. Rev. Lett. **123**, 225001 (2019).
[23] C.-S. Wong, J. Goree, Z. Haralson, and B. Liu, Nat. Phys. **14**, 21 (2018).
[24] Y. Feng, J. Goree, and B. Liu, Phys. Rev. Lett. **104**, 165003 (2010).
[25] D. Samsonov, S. K. Zhdanov, R. A. Quinn, S. I. Popel, and G. E. Morfill, Phys. Rev. Lett. **92**, 255004 (2004).
[26] A. Melzer, S. Nunomura, D. Samsonov, Z. W. Ma, and J. Goree, Phys. Rev. E **62**, 4162 (2000).
[27] V. Nosenko, S. K. Zhdanov, A. V. Ivlev, C. A. Knapek, and G. E. Morfill, Phys. Rev. Lett. **103**, 015001 (2009).
[28] L. Couëdel, V. Nosenko, M. Rubin-Zuzic, S. Zhdanov, Y. Elskens, T. Hall, and A. V. Ivlev, Phys. Rev. E **97**, 043206 (2018).
[29] C. A. Knapek, D. Samsonov, S. Zhdanov, U. Konopka, and G. E. Morfill, Phys. Rev. Lett. **98**, 015004 (2007).
[30] T. E. Sheridan, V. Nosenko, and J. Goree, Phys. Plasmas **15**, 073703 (2008).
[31] R. Heidemann, S. Zhdanov, R. Sütterlin, H. M. Thomas, and G. E. Morfill, Phys. Rev. Lett. **102**, 135002 (2009).
[32] W. Sun, M. Schwabe, H. M. Thomas, A. M. Lipaev, V. L. Molotkov, V. E. Fortov, Y. Feng, Y.-F. Lin, J. Zhang, Y. Guo *et al.*, Europhys. Lett. **122**, 55001 (2018).
[33] X.-R. Hong, W. Sun, M. Schwabe, C.-R. Du, and W.-S. Duan, Phys. Rev. E **104**, 025206 (2021).
[34] C. Killer, T. Bockwoldt, S. Schütt, M. Himpel, A. Melzer, and A. Piel, Phys. Rev. Lett. **116**, 115002 (2016).
[35] D. Samsonov, A. V. Ivlev, R. A. Quinn, G. Morfill, and S. Zhdanov, Phys. Rev. Lett. **88**, 095004 (2002).
[36] P. Harvey, C. Durniak, D. Samsonov, and G. Morfill, Phys. Rev. E **81**, 057401 (2010).
[37] L. Couëdel, V. Nosenko, A. V. Ivlev, S. K. Zhdanov, H. M. Thomas, and G. E. Morfill, Phys. Rev. Lett. **104**, 195001 (2010).
[38] V. Nosenko, G. E. Morfill, and P. Rosakis, Phys. Rev. Lett. **106**, 155002 (2011).

[39] Y. Ivanov and A. Melzer, Rev. Sci. Instrum. **78**, 033506 (2007).
[40] Y. Feng, J. Goree, and B. Liu, Rev. Sci. Instrum. **78**, 053704 (2007).
[41] F. Wieben and D. Block, Phys. Plasmas **25**, 123705 (2018).
[42] S. Nunomura, J. Goree, S. Hu, X. Wang, and A. Bhattacharjee, Phys. Rev. E **65**, 066402 (2002).
[43] L. Couëdel, V. Nosenko, S. K. Zhdanov, A. V. Ivlev, H. M. Thomas, and G. E. Morfill, Phys. Rev. Lett. **103**, 215001 (2009).
[44] A. V. Ivlev, U. Konopka, and G. Morfill, Phys. Rev. E **62**, 2739 (2000).
[45] A. Melzer, V. A. Schweigert, and A. Piel, Phys. Rev. Lett. **83**, 3194 (1999).
[46] R. Kompaneets, G. E. Morfill, and A. V. Ivlev, Phys. Rev. Lett. **116**, 125001 (2016).
[47] K. Jiang and C.-R. Du, Rev. Mod. Plasma Phys. **6**, 23 (2022).
[48] A. V. Ivlev, J. Bartnick, M. Heinen, C.-R. Du, V. Nosenko, and H. Löwen, Phys. Rev. X **5**, 011035 (2015).
[49] M. Fruchart, R. Hanai, P. B. Littlewood, and V. Vitelli, Nature (London) **592**, 363 (2021).
[50] A. Homann, A. Melzer, S. Peters, R. Madani, and A. Piel, Phys. Lett. A **242**, 173 (1998).
[51] V. Nosenko, S. Nunomura, and J. Goree, Phys. Rev. Lett. **88**, 215002 (2002).
[52] A. Ashkin, Phys. Rev. Lett. **24**, 156 (1970).
[53] Y.-F. Lin, A. Ivlev, H. Löwen, L. Hong, and C.-R. Du, Europhys. Lett. **123**, 35001 (2018).
[54] S. Plimpton, J. Comput. Phys. **117**, 1 (1995).
[55] A. P. Thompson, H. M. Aktulga, R. Berger, D. S. Bolintineanu, W. M. Brown, P. S. Crozier, P. J. in 't Veld, A. Kohlmeyer, S. G. Moore, T. D. Nguyen *et al.*, Comput. Phys. Commun. **271**, 108171 (2022).
[56] A. Boruah, S. K. Sharma, Y. Nakamura, and H. Bailung, Phys. Plasmas **23**, 093704 (2016).
[57] H. Edelsbrunner, D. Kirkpatrick, and R. Seidel, IEEE Trans. Inf. Theory **29**, 551 (1983).
[58] A. W. Baggaley, Phys. Rev. E **91**, 053019 (2015).
[59] D. J. Skinner, B. Song, H. Jeckel, E. Jelli, K. Drescher, and J. Dunkel, Phys. Rev. Lett. **126**, 048101 (2021).
[60] H. Tong and H. Tanaka, Nat. Commun. **10**, 5596 (2019).
[61] H. Tong and H. Tanaka, Phys. Rev. Lett. **124**, 225501 (2020).
[62] H. Tanaka, H. Tong, R. Shi, and J. Russo, Nat. Rev. Phys. **1**, 333 (2019).